Strategic Synthesis of Heptacoordinated FeIII Bifunctional Complexes for Efficient Water Electrolysis

A Journal of the Gesellschaft Deutscher Chemiker

Angewandte International Edition GDCh Chemie

www.angewandte.org

Accepted Article

Title: Strategic Synthesis of Heptacoordinated Fe(III) Bifunctional Complexes for Efficient Water Electrolysis

Authors: Abhishikta Chatterjee, Dr. Papri Mondal, Priyanka Chakraborty, Bidyapati Kumar, Sourav Mondal, Prof. Corrado Rizzoli, Dr. Rajat Saha, Prof. Bibhutosh Adhikary, and Subrata K. Dey

To be cited as: *Angew. Chem. Int. Ed.* **2023**, e202307832

Link to VoR: https://doi.org/10.1002/anie.202307832

WILEY VCH

10.1002/anie.202307832

WILEY-VCH

RESEARCH ARTICLE

Strategic Synthesis of Heptacoordinated Fe(III) Bifunctional Complexes for Efficient Water Electrolysis

Abhishikta Chatterjee[a], Papri Mondal[b], Priyanka Chakraborty[a], Bidyapati Kumar [a], Sourav Mandal[a], Corrado Rizzoli[c], Rajat Saha[d], Bibhutosh Adhikary[b], Subrata K. Dey[a,*]

[a] Abhishikta Chatterjee, Priyanka Chakraborty, Bidyapati Kumar, Sourav Mondal, Prof. Subrata K. Dey
Department of Chemistry
Sidho-Kanho-Birsha University, Purulia-723104, WB, India
E-mail: skdchem@skbu.ac.in
[b] Dr. Papri Mondal, Prof. Bibhutosh Adhikary
Department of Chemistry
Indian Institution of Engineering Science and Technology, Shibpur, Howrah, India
[c] Prof. Corrado Rizzoli
Dipartimento S.C.V.S.A.
Università di Parma, Parco Area delle Scienze 17/A, Parma I-43124, Italy
[d] Dr. Rajat Saha
Department of Chemistry, Kazi Nazrul University, Asansol-713340, WB, India

Abstract: In this research, highly efficient heterogeneous bifunctional (BF) electrocatalysts (ECs) have been strategically designed by Fe coordination (C_R) complexes, $[Fe_2L_2(H_2O)_2Cl_2]$ **(C1)** and $[Fe_2L_2(H_2O)_2(SO_4)].2(CH_4O)$ **(C2)** where the high seven C_R number synergistically modifies the electronic environment of the Fe centre for facilitation of H_2O electrolysis. The electronic status of Fe and its adjacent atomic sites have been further modified by the replacement of $-Cl^-$ in **C1** by $-SO_4^{2-}$ in **C2.** Interestingly, compared to **C1**, the O-S-O bridged **C2** reveals superior BF activity with extremely low overpotential (η) at 10 $mAcm^{-2}$ (140 mV_{OER}, 62 mV_{HER}) and small Tafel slope (120.9 $mVdec^{-1}{}_{OER}$, 45.8 $mVdec^{-1}{}_{HER}$). Additionally, **C2** also facilitates a high-performance alkaline H_2O electrolyzer with cell voltage of 1.54 V at 10 $mAcm^{-2}$ and exhibits remarkable long-term stability. Thus, exploration of the intrinsic properties of metal-organic framework (MOF)-based ECs opens up a new approach to the rational design of a wide range of molecular catalysts.

Introduction

According to the report of the International Energy Agency, global energy demand will expand by 30% and CO_2 generation will reach 35.7 Gt $year^{-1}$ by 2040.[1,2] Accordingly, the researchers worldwide have been working on developing clean and sustainable renewable energy conversion-storage technologies.[3,4] To reduce the carbon footprint, electrochemical H_2O splitting into O_2 (OER) and H_2 (HER) is currently a hot research topic.[5,6] The key aspect for scalable O_2 and H_2 production is developing highly-efficient yet low-cost BF ECs with lower η.[7-10] The first row transition metals, specially Fe, stand out as promising catalysts in the field of electron transfer reactions due to their Lewis acid character, facile change of oxidation state, and relatively nontoxic nature. Recently, Fe coordination compounds[11] have attracted intense research attention for not only their environment friendly nature, abundance, and inexpensiveness, but also for their ability to meet the high thermodynamic H_2O oxidation potential (1.23 V_{NHE}).[12]

The choice of redox active multivalent metal centres and oxidatively rugged ligands is one of the key strategies for the fabrication of durable efficient complexes that behave as BF electrocatalysts.[13] Generally, imine or amido ligands with nitrogen donors and alkoxide ligands with oxygen donors are used as H_2O splitting catalyst (WSCs) due to their capability of stabilizing the higher oxidation states of metal centres as well as their superior catalytic cycling stability.[14-17] Since the first well characterized molecular WSC, the so called Ru ''blue dimer'', many research studies have confirmed that a dinuclear electrocatalyst providing a two-site platform acts as an excellent choice for the development of WSCs due to its synergic effects and cooperative mechanisms compared to mononuclear complexes which deactivate rapidly.[18] To achieve useful WSCs, numerous efforts have already been made by the researchers.[13a, 17] In 2014, Najafpour *et. al.,* first reported that dinuclear Fe complex is six times more efficient than mononuclear Fe complex with Ce^{IV} as oxidant.[19] Ma *et al.* also demonstrated that the μ-(oxo)-μ-(acetato) form of a diiron complex is an active species responsible for H_2O oxidation compared to its monomer.[20] In 2016, Åkermark *et al.* reported the targeted synthesis of a Fe-based system with pre-organised ligand framework as an efficient catalyst and showed how nuclearity induces these systems to function as WSCs.[14c] In 2020, Das *et al.* reported OER from a dimeric Fe complex where the replacement of labile Cl^- by OH^-, lead to the generation of peroxo- bridged Fe^{III} during the water oxidation process.[21] Interestingly, Que *et al.* reported a diiron complex formed by a pentadentate ligand which can activate the H_2O molecule *via* proton-coupled electron transfer, but the generated hydroxyl radical is consumed by the solvent moiety so that O_2 cannot be detected.[22] In a recent study Masaoka *et al.* developed an efficient pentanuclear Fe complex with TOF of 1900 s^{-1},[23] but the formed high valent Fe=O can abstract the H atom from the ligand moiety. Therefore, these Fe-based molecular catalysts pose a great challenge on their stability.[24] Accordingly, the exploitation of effective heterogeneous molecular WSCs is a promising strategy to achieve catalysts with enhanced atom-efficiency and large-scale applications.

Herein, we present two new dinuclear Fe complexes $[Fe_2L_2(H_2O)_2Cl_2]$ (**C1**) and $[Fe_2L_2(H_2O)_2(SO_4)].2(CH_4O)$ **(C2)** as efficient OER/HER

electrocatalysts where C2 exhibits efficient BF OER/HER performances as well as excellent long-term stability with ultra-low η, high current density, and low Tafel slope. Moreover, the excellent bifunctional catalytic activity of C2 inspired us to assemble a symmetric alkaline H_2O electrolyzer with C2 as both anode and cathode material, where the bridging SO_4^{2-} group probably assists to substantially decrease η for OER/HER, thereby promoting overall H_2O electrolysis. To the best of our knowledge, such a kind of complex EC has not been reported yet. Owing to appropriate structural conformation, ligand effect, large electrochemical active surface area (ECSA), efficient active sites, excellent conductivity, and superior stability, it offers the remarkable multifunctional activity of a well-designed heterogeneous molecular catalyst which can be reproduced easily for a broad range of applications.

In order to eliminate the major challenges of electrocatalysis *e. g.,* high activation energy barrier, poor catalytic durability, redox balancing, several redox processes between the metal centres, [25-28] etc., we have strategically designed these types of dinuclear catalysts taking into account the following targets: (i) excellent stability of molecular WSCs by tuning the electronic/steric properties of the ligand which requires meticulous screening depending upon its nature, (ii) arrangement of a pre-organised ligand by developing higher C_R as well as multinuclear complexes to increase the electronegativity and subsequent activity of the metal centre which facilitates the H_2O splitting, (iii) subsequent replacement of the $-Cl^-$ ions by a bridging $-SO_4^{2-}$ ion for delocalization of the electron density over the molecular catalyst, and (iv) development of abundant active sites with modified electron density for favourable adsorption of H_2O splitting intermediates.

The detailed investigation of the electronic properties of **C1** and **C2** reveals a strong dependence of their electrocatalytic activity on the coordinated ligands which subsequently alter the electronic status of Fe centres. The hepta coordination and O-S-O bridging $-SO_4^{2-}$ in **C2** offer highly favourable new physicochemical properties with modulated electronic configuration which provides abundant active sites and faster mass-charge transportation, thereby resulting an ultra-high BF catalytic activity and strong durability toward overall H_2O splitting (OWS). Thus, this work reports a new cost-effective molecular catalyst where the ligand structure tunes its catalytic performances.

Results and Discussion

An exhaustive search of iron coordination complexes revealed that 0.7% of all iron compounds exhibit the coordination number seven. Of all the *hepta*-coordinate complexes 23 are dinuclear, among these 13 correspond to Fe(III) systems having pentagonal bipyramidal (PBP) coordination geometry around the central metal and only a few heptacoordinated diiron (III) complexes containing alkoxide and μ-sulphate bridge are reported in the literature to date.[29-42] Herein two new diiron complexes with a preorganised ligand (L, S1.1.) are reported, both of which have been characterized by single crystal structural studies.[29] The dinuclear complexes exhibit seven-coordinated Fe^{III} centers where the bridge is an alkoxide group (**C1**, Section S1.2) or an alkoxide group and a sulphate group (**C2**, Section S1.3). The preliminary IR spectroscopic characterizations of **C1** and **C2** (Figures S2a and S2b) clearly indicate that their characteristic peaks are in accordance with the results of the single crystal analyses.

The structural details of **C1** (Figure 1a) are listed in Section S1.4 and Table S7. Selected bond lengths and bond angles are summarized in Table S8. The complex molecule of **C1** has crystallographically imposed inversion symmetry, the symmetry centre being located at the midpoint between adjacent Fe atoms. During the metalation, the ester group of the ligand hydrolyzed to COO^-. The two metal centres are bridged by the deprotonated alkoxide oxygen atoms of two tetradentate Schiff base ligands (L). The four donor atoms from one ligand are a pyridine nitrogen (N1), an imino nitrogen (N3), a μ_2-bridging alkoxide atom (O2) and an acetate oxygen atom (O1) from the hydrolyzed ethyl pyruvate moiety. The central Fe_2O_2 core is slightly asymmetric with Fe1–O1 = 2.119(3) Å and Fe1–$O1^i$ = 2.083(3) Å (i = 1-x, 1-y, 1-z). The distance between the Fe^{III} atoms is 3.5414(7) Å. The bridging Fe1–O1–$Fe1^i$ angle is 114.85(12)°. The longest Fe–O bridging alkoxide bond is *trans* to the acetate oxygen atom O1 and the shortest Fe–O bond is *trans* to the imino nitrogen atom (N3). Each Fe^{III} atom displays an unusual pentagonal bipyramidal coordination geometry. The equatorial plane (r.m.s. deviation = 0.0727 Å) is formed by the two bridging alkoxide oxygen atoms (O2, $O2^i$), two nitrogen atoms (N1, N3) and one carboxylate oxygen atom (O1) and the axial sites are occupied by a chloride ion and the oxygen atom of a H_2O molecule. The bond angles around the Fe^{III} involving adjacent donor atoms in the pentagonal equatorial plane are in the range from 65.15(12) to 81.34(12)° (mean value 72(3)°). Bond valence sum calculation suggests that Fe is in the +3-oxidation state. Each ligand contains two easily dissociable protons connected with the hydrazone and pyruvate fragments along with one negative charge generated by the hydrolysis of terminal carboxylic ester function. The overall charge balance for the **C1** with two Fe^{III} metal centres is ensured by four negative charges spread out over the two ligands and two negative charges by two Cl^- ligand, thereby resulting in a neutral complex. H-bonding plays a pivotal role in the stabilization of the crystal packing, molecules interacting through classical O–H…O and O–H…Cl hydrogen interactions involving the H_2O molecule, the Cl^- and the O4 carboxylate oxygen atom to form layers running parallel to (0 1 0) (Table S9, Section S2.10; Figure S14).

The structure of **C2** is illustrated in Figure 1b, details on the single crystal X-ray crystallographic analysis are listed in Table S7 (Section S1.4) and selected bond lengths and angles are listed in Table S10. The complex molecule has crystallographic imposed C_2 symmetry, the two-fold axis being coincident with the normal to the midpoint of the Fe…Fe line. The sulphate anion

10.1002/anie.202307832

(SO_4^{2-}) is disordered over two orientations about the two-fold axis sharing the O5 and $O5^i$ oxygen atoms (i = 1-x, y, 0.5-z).

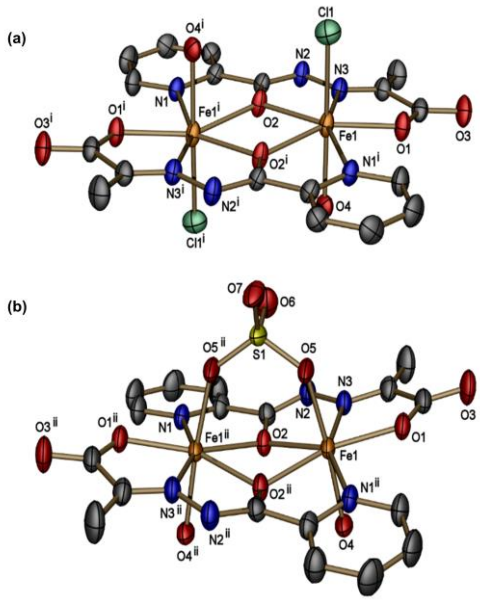

Figure 1. The structure of (a) **C1** and (b) **C2** with displacement ellipsoids drawn at 40% probability level. Hydrogen atoms are omitted for clarity. Only one orientation of the disordered SO_4^{2-} in **C2** is shown. Symmetry codes: (i) 1-x, 1-y, 1-z; (ii) 1-x, y, 0.5-z.

The structure of the complex closely resembles that of **C1**, and consists of two crystallographically-related ligands bridging two Fe atoms through the deprotonated alkoxide oxygen atoms (O2, $O2^{ii}$; ii = 1-x, y, 0.5-z). The hydrolyzed unsymmetrical ditopic ligand exists in a doubly deprotonated form resulting in a *homo*-valent Fe dinuclear complex. It is worth mentioning that the ester hydrolysis of the ligand takes place in order to fulfil the electrophilicity of the two Fe^{III} centres. The seven-coordinated Fe atoms display a slightly distorted (N2O5) pentagonal bipyramidal coordination geometry, with O_2 alkoxide oxygen atom, N1 pyridine nitrogen, N3 imino nitrogen atom and one carboxylate oxygen atom (O1) forming the equatorial plane (r.m.s. deviation = 0.0684 Å), and with the axial sites occupied by the oxygen atoms of a H_2O molecule (O4) and of the bridging $-SO_4^{2-}$ (O5). The Fe…Fe separation is 3.4633(19) Å, in close agreement with the value observed for **C1**, the bond angles around the Fe involving adjacent donor atoms in the equatorial plane are in range from 65.07(15) to 81.22(14)° (mean value 72(3)°). The bridging O_2 alkoxide atoms bind almost symmetrically the Fe centres (Fe1–O_2 = 2.105(4) Å, Fe1–O_2^{ii} = 2.097(4) Å), and the Fe–O–Fe^{ii} angles are 111.04(15)°. The Fe–O bond lengths involving $-SO_4^{2-}$ (Fe1–O5 = 1.975(3) Å) are significantly shorter than those involving H_2O molecule (Fe1–O4=2.019(4) Å). The overall charge balance for the two Fe^{III} metal centres in **C2** is ensured by four negative charges spread out over the two ligands and two negative charges by one bridging SO_4^{2-}. The packing arrangement of **C2** is governed by OH…O hydrogen bonds (Table S11, Section S2.10; Figure S15) between the uncoordinated MeOH molecules and the axially coordinated H_2O forming layers parallel to (1 0 1). H_2O molecules in **C1** and **C2** bind in an *anti*- fashion and *syn*-fashion, respectively, which leads to the difference in C_R geometry as well as catalytic efficiency of these two complexes.

In order to get a clear insight into the morphology of **C1** and **C2**, scanning electron microscopic (SEM, Section S1.5) analysis was performed. **C1** exhibits a uniform prominent edged layered morphology which looks like skin shell (Figure S12a) while **C2** adopts a butterfly type with noticeably high surface area (Figure S13a). Subsequently, to measure their catalytically active surface area and confirm their surface accessibility, ECSA (Eq. S12) and roughness factor (R_f) (Eq. S13) were calculated from electrochemical impedance spectroscopic (EIS) techniques (Figures S4 and S5) for both OER (at η of 130 mV) and HER (at η of 49 mV) (Table 1). The double layer capacitance (C_{dl}) (from Randles cell model; Figure S1) for both ECs, obtained from EIS were used to evaluate the ECSA where **C2** was observed to exhibit a greater ECSA for both OER (101.0 m^2/g) and HER (121.8 m^2/g) than **C1**, indicating that the surface of **C2** was highly enriched with active sites which may contribute to its enhanced electrocatalytic performances.

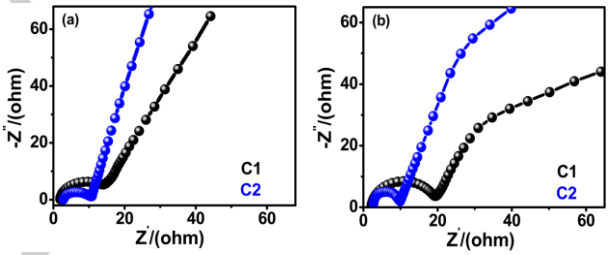

Figure 2. EIS of **C1**, and **C2** in 1.0 M KOH under 1600 rpm rotational speed at η of (a) 130 mV in OER, and (b) 49 mV in HER.

Interestingly, replacing the $-Cl^-$ substituents in **C1** by $-SO_4^{2-}$ (**C2**), a noticeable raise of R_f (Table 1) was observed during both OER/HER, thus changing the catalytic activity of ECs. This sharp increase of surface roughness of **C2** for both OER (1924.6) and HER (2321.4) is expected to capably facilitate ion-gas transportation thereby contributing to its highest electrocatalytic OER/HER performances. Therefore, the order of active site density and R_f values certainly verifies the activity pattern of the two ECs as well as offers a probable indication of the fundamental basis for the catalytic enrichment of **C2**.

The electrochemical experiments were carried out on a CHI7014E electrochemical analyser (CH Instruments, USA) using a rotating disc electrode (RDE) in a standard three electrode cell configuration at room temperature. The RDE (disk diameter 4 mm), Ag/AgCl electrode (with saturated KCl solution), and a graphite rod were employed as working, reference, and counter electrodes, respectively. Throughout all the experiments, purified 1.0 M aqueous KOH solution (pH ~11.6) was used and this electrolyte was purged with high–purity N_2 over 30 min before OER and HER measurements. All electrochemical

10.1002/anie.202307832

performances were completed under a rotational speed of 1600 rpm. For comparative study, blank experiments for OER and HER were also performed (Figure S3).

Table 1. Surface Parameters of the ECs during OER and HER

Materials	Mass Loading (mg cm^{-2})	Charge Transfer Resistance (R_{ct}) (Ω)	C_{dl} (mF cm^{-2})	ECSA (m^2/g)	R_f
OER					
C1	~ 0.24	11.8	3.4	35.4	674.6
C2		7.8	9.7	101.0	1924.6
HER					
C1	~ 0.24	17.2	0.8	8.3	158.7
C2		6.9	11.7	121.8	2321.4

Initially, RDE was sequentially cleaned with 0.5 and 0.05 μm alumina powder and then washed with H_2O under sonication for 30 min. The working electrode for both OER/HER was prepared as follows: ~6.2 mg of complex EC was dispersed well for 1 h through ultrasonication into the mixture of 1 mL of H_2O and 40 μL of nafion (0.5 %) to produce a homogeneous ink. Subsequently, 5 μL of the prepared ink was drop–casted on the prepolished glassy carbon disk of RDE, resulting in an EC loading 0.24 mg cm^{-2}. Finally, the prepared electrodes were air–dried for 2 h at room temperature for all electrochemical measurements (Section S1.6).

To investigate the electrocatalytic H_2O oxidation ability of the complexes, linear sweep voltammetry (LSV) was initially carried out. Figure 3a illustrates that both ECs (Section S1.7) possess H_2O oxidation capability where, interestingly, the OER polarization curve of **C2** displays a negative shifted onset potential (Figure 3b) of 30 mV compared to **C1**. Moreover, the significant smaller OER overpotential (η_{10}) (Eq. S1) of 1.37 V at 10 mA cm^{-2} of **C2** compared to **C1** further confirms its superiority in electrocatalysis (Figure 3b, Table S2). The overpotential (η_{20}) also shows a similar trend where **C2** possessed a much smaller value (180 mV) that is 50 mV lower than **C1** (Table S2). Furthermore, the evolution current density of **C2** was found to reach 344.6 mA cm^{-2} (Table S2, Figure 3c) at η of 570 mV which is also noticeably better than that observed for **C1** (254.0 mA cm^{-2}), revealing the rapid e^- transfer rate between electrolyte and EC (C2) surface. Thus, the above results prove the efficiency of the heptacoordinated dinuclear Fe complexes toward H_2O oxidation as well as the significant role played by the ligand substitution for the distinctive improvement of OER performances (Section S1.10).

Even though η is an advantageous performance index for OER ECs, it is materially a key parameter whose value depends on the mass loading of the EC on electrode surface. To eliminate the effect of mass loading, the catalytic activity of the ECs was investigated on the basis of mass–normalized current density (j_m). A quite small η (190 mV) is needed for **C2** to attain a current density of ~100 A g^{-1} which is smaller than that required for **C1** (240 mV) (Figure 3d). Evidently, this mass activity (Eq. S14) trend further agrees well with that of η_{10} and η_{20} where **C2** largely outperforms **C1** exhibiting high mass activity of 220.0 A g^{-1} at 1.48 V (Figure 3e). Thus, the significant enhanced OER performance of **C2** was further verified by the mass activity determination that gives much pronounced activity differences between the ECs.

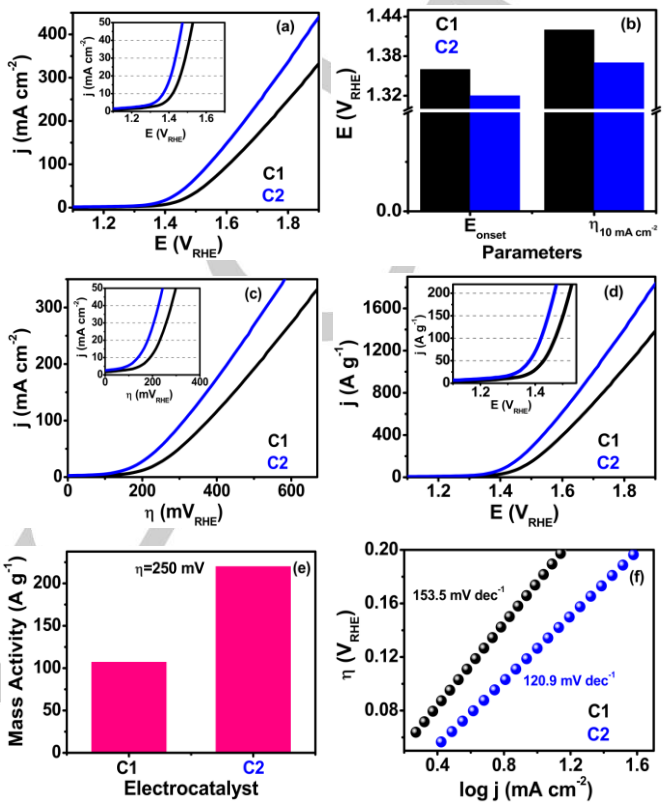

Figure 3. (a) OER polarization curves in 1 M KOH under 1600 rpm rotational speed (inset, LSV plot up to current density of 50 mA cm^{-2}), (b) bar diagram representing E_{onset} and $\eta_{10\ mA\ cm^{-2}}$, (c) the current density vs. η plots (inset, LSV plot up to current density of 50 mA cm^{-2}), (d) mass activity plots (inset, plot up to current density of 220 A g^{-1}), (e) bar diagram of mass activity at η=250 mV, and (f) OER Tafel plots of **C1** and **C2**.

In addition, Tafel plots were also used to obtain deeper information about reaction kinetics. Figure 3f depicts the lower Tafel slopes of **C2** compared to **C1** (Eq. S2, Table S2), revealing the more efficient and faster OER kinetics which is properly reflected on the superior catalytic efficiency of **C2**. Moreover, this smallest slope of **C2** reflects its superior electrical conductivity and efficient charge transfer ability. Thus, once again, the activity enhancement of the EC shows a clear dependence on the complex structure as well as ligand substitution and the superior OER performance of **C2** offers strong evidence for this fact.

Dinuclear WSCs are generally believed to follow the I2M mechanism, although some exceptions exist [23]. In dinuclear systems, the I2M mechanism is accompanied by the *in-situ* generation of metal dimers via coupling of metal-oxo species. Two H_2O molecules in **C1** bind in an *anti*-fashion whereas in **C2,** these two H_2O bind in *syn*-fashion with respect to the diiron vector. Particularly these difference in ligand flexibility, C_R geometry and availability of H_2O molecules

provide a research platform for understanding the relationship between structure and catalytic activity. The overall experimental result indicates that the replacing of the $-Cl^-$ substituent by the $-SO_4^{2-}$ ion in Fe based dinuclear complex predominantly contributes to the enhanced OER activity of **C2** thereby regulating its surface electronic status as well as electrical conductivity. The catalytic cycle of H_2O oxidation on EC surface is presented in Scheme S1 (Section 2.11, Eq. S3-S7) with the deprotonation sites emphasized and O-O bond formation proposed by S. Masaoka, *et al.*[23]. In alkaline media, the probable initial state of **C1** and **C2** would be HO-$Fe^{III}(L_2)Fe^{III}$-OH due to the strong acidity of Fe^{III}-OH_2 (Scheme S1). As both Fe^{III} centres possess similar ligand environments, in Step-I, deprotonation from one OH molecule attached to any Fe^{III} leads to the oxidation of Fe^{III} to Fe^{IV} in the dinuclear Fe complex[43] .The second deprotonation occurs from other OH anion leading to the formation of Intermediate 1 (Int 1, Section S2.11) in Step-II. Now, Int 1 may undergoes two probable pathways. In Pathway **1** (Step-III), a H_2O molecule coordinates to one of the Fe^{IV}(=O) site in concert with the transfer of a proton to the (=O) group attached to the other Fe^{IV} site thereby changing the oxidation state of both Fe^{IV} to Fe^{III}. In Step-IV, a deprotonation occurs at the Fe^{III}-O-O-H site which facilitates the release of O_2 in final Step-V. Alternatively (Pathway 2), after losing two electrons and two protons, the two Fe^{IV}(=O) moieties of Int 1 (Step-II) with *syn*-position for **C2** can directly couple with each other to trigger the O-O bond formation *via* intramolecular oxo/oxo coupling (Step-III′). What requires to be mentioned here is that the O-O bond formation needs the *anti*- to *syn*-configuration conversion between two Fe^{IV}(=O) moieties. Thus, two *anti*-typed Fe^{IV}(=O) moieties in **C1** cannot catalyse the O-O bond formation through a similar pathway, as they should need to be further oxidized to higher valent Fe^{V}(=O) intermediate. After the O-O bond formation, the obtained EC intermediate could be further oxidized to liberate O_2 (Step-IV′) through closing the catalytic cycle. This mechanistic difference (Pathway 2) provides a strong clue for the much higher catalytic activity of **C2** compared to **C1** which illustrates the greater possibility and predominancy of Pathway 2.

The Tafel slopes are used to evaluate the rate determining steps of the adsorbed species ($\theta \approx 0$ or ≈ 1), although, in practice, the slopes are coverage-dependent. The OER is known as a 2 or 4 electron step and the reaction mechanism is complicated. Based on the literature, considering OER is the backward reaction of oxygen reduction reaction, we have proposed OER mechanistic pathway given in SI (Scheme S1) under alkaline conditions. According to Tafel plots, a Tafel slope of 120 mV dec^{-1} was observed for **C2** which reveals that the surface species formed in the step just before the rate-determining step (RDS) is predominant. When the surface adsorbed species produced in the early stage of OER remains predominant, the Tafel slope decreases [43].

The substituent variations, i.e., replacement of $-Cl^-$ by $-SO_4^{2-}$ of our dinuclear Fe complexes, lead **C2** to be a more OER active than **C1** as the catalytic efficiency of C_R complex-based EC strongly depends on their electronic properties, surface affinity, and steric bulkiness. Most importantly, hydrophobicity was recognized as the vital variable in mediating the catalytic competency of transition metal complexes. The alteration in this parameter connects both with the conformational mobility of the ligand core and the structural changes in the local solvent environment around the catalytic metal site. A significantly lower onset potential (1.33 V) and η_{10} (0.14 V) (Table S2) was attained by **C2** compared to **C1** due to the more substantial electron-withdrawing ability of the substituents ($-SO_4^{2-}$) in **C2**, leading **C2** to be more hydrophobic in nature.

Such designed dinuclear Fe complexes of Schiff base ligands with four donor atoms, i.e., one pyridine nitrogen, one imino nitrogen, one bridging μ_2-alkoxido atom and one oxygen, are becoming more advantageous for both **C1** and **C2**, specially for **C2** containing the more electron-withdrawing $-SO_4^{2-}$ substituent, for accelerating a H_2O oxidation reaction through lowering the activation energy barrier. As designed in Scheme S1, while two terminal Fe^{IV}=O moieties initially locate at *anti* position in the intermediate stage, they could get close to each other by rotating axially around the Fe-O-Fe bonds and further couple in a relatively flexible structure. When the molecular structure becomes rigid, the rotation of Fe^{IV}=O will be limited, making them difficult to couple face-to-face, and the catalyst would exhibit a lower activity. Moreover, the two H_2O molecules in **C2** placed in *syn*-position, can directly couple with each other to form O-O bond, enhancing the activity of the complex.[44] This superior efficiency may be attributed to the following phenomena: EC offers (i) highly available catalytic active sites which assist the selective adsorption of oxygenated intermediates to a particular site; (ii) good permeability of the ions through distinct channels of mesoporous structure thereby resulting in a faster mass transportation; (iii) excellent surface accessibility of OH^- ions; (iv) favourable charge transportation due to the exceptional redox features of Fe^{III} ; (v) variable oxidation state of the Fe centres where Fe^{III} can readily transform to Fe^{III}/Fe^{IV} during OER reactions; and (vi) rapid e^- transfer with relatively low activation energies thereby enhancing electronic conductivity. Therefore, the overall result proves that the redox active property and C_R environment of Fe^{III}, presence of redox-active Schiff-base ligands, porosity, and dimensionality of the networks in the complex structure greatly facilitates the electrocatalytic efficiency of **C2** through speeding up the H_2O oxidation reaction. All the predominant factors toward enhanced OER performance of **C2** were established by the following results:

(i) EIS: The electrode kinetics and structural characteristics of the ECs were examined by EIS technique (Figure 2a). To gain deeper insight into the obtained Nyquist plot, an equivalent Randles cell model has been used (Section S2.1,

10.1002/anie.202307832

Figure S1). Table 1 illustrates the lower R_{ct} value of **C2** compared to **C1** and thus the smallest R_{ct} for **C2** confirms the rapid charge transport kinetics revealing faster e^- transfer between EC and substrate, further verifying the admirable efficiency of **C2** in boosting the OER activity.

Additionally, **C2** was also found to exhibit the higher C_{dl} value of 9.7 mF cm^{-2} (Table 1) which is ~ 3 times larger than C1. This result signifies the largest effective ECSA (Section S1.12, Eq. S12) of **C2** which can offer abundant active sites and rough catalytic surface leading to excellent OER performance (Table S2).

(ii) Turn Over Frequency (TOF): The intrinsic OER activity was also investigated through TOF calculation (Section S1.12, Eq. S15), assuming all metal atoms involved in OER. The result reveals that the greater TOF value (0.24 s^{-1}) of **C2** which is almost 2.2–fold larger than that of **C1** (0.11 s^{-1}) at η of 240 mV which strongly contributes to the remarkable OER performance of **C2.** This highest TOF may offer a strong sign about the enriched and much exposed active sites as well as superior conductivity of **C2**.

(iii) Ligand Effect: The remarkable activity of **C2** may be strongly attributed to the ligand effect where $-SO_4^{2-}$ ligand in **C2** forms an -O-S-O- bridge between two Fe centre that facilitates the intramolecular oxo-oxo coupling through formation of two *syn* Fe^{IV}=O moiety leading to O-O bond formation (Scheme S1). In contrast, the two *anti*-positioned $-Cl^-$ ligands in **C1** lead to the formation of two *anti* Fe^{IV}=O moieties that hinder the oxo-oxo coupling *via* Pathway 2 (Scheme S1).

(iv) Structural Conformation: The two *syn* Fe^{IV}=O moieties in **C2** (supported by Figure 1b and Scheme S1) facilitate the intramolecular oxo–oxo coupling leading to O-O bond formation (Scheme S1, Pathway 2) which predominantly contributes to its higher electrocatalytic OER activity rather than the O-O bond formation by H_2O nucleophilic attack (Scheme S1, Pathway 1). Importantly for **C1**, the structural rigidity restricts the *anti* to *syn* isomerization and axial rotation of the Fe^{IV}=O moieties (supported by Figure 1a), making them difficult to couple face-to-face leading to a lower catalytic activity. But interestingly Pathway 2 probably contributes to the resultant OER activity of **C1**.

Thus, the ligand effect with complementary electronic properties and structural conformation synergistically enhances the OER performance of **C2** in comparison to **C1**. Moreover, among the earth abundant transition metal based OER ECs, Fe-based ECs have attracted a great attention owing to their interesting electronic and redox properties as well as the anticipated high synergistic effect with the coordinating heteroatom ligands which can significantly modify the surface properties of the EC facilitating the electrocatalysis. Therefore, the comparative study of OER activity of the dinuclear complex reveals the importance of the synergistic effect among two dinuclear homometallic centres and Schiff-base ligand which leads to more surface-active metal sites and an enhanced electron rich environment, both of which are advantageous for superior OER catalytic performance.

In addition to specific activity, long-term durability has also a great significance in their practical utility. Therefore, the catalytic stability of both ECs was examined by chronopotentiometric study at constant current of 10 mA cm^{-2}. Figure 4a depicts the superior stability of **C2** with very small increase of η while **C1** showed a noticeable increase of η (~30 mV) after 24 h. This result was also confirmed by cycling stability test [Figures 4(b,c)] where E_{onset} (Figure 4d) exhibits a similar activity trend. Moreover, the insignificant change of η_{10} for **C2** (0.14 to 0.15 V) compared to **C1** (0.19 to 0.21 V) after 5000 cycles further strongly supports the more sustained and superior activity of **C2** over long catalytic reaction periods (Figure 4e). Moreover, Figure 4f also depicts a smaller increase of Tafel slope from 120.9 to 129.3 mV dec^{-1} for **C2** after stability test, while the slope of **C1** was found to increase significantly (Table S2), reflecting the much faster deactivation of **C1** over time. The EIS result of **C2** (Section S2.2, Figure S4b) after stability test may perhaps offer a strong support toward its superior stability thereby exhibiting very little change of R_{ct} while a noticeable increase of R_{ct}, was observed for **C1** (Section S2.2, Figure S4a).

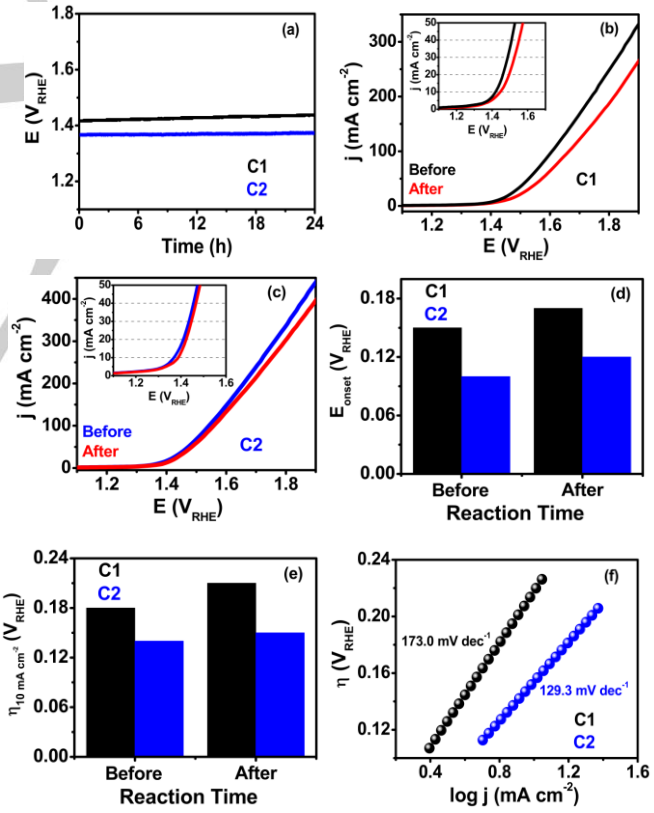

Figure 4. (a) Chronopotentiometric measurements of ECs at 10 mA cm^{-2} for 24 h in 1 M KOH under 1600 rpm rotational speed; OER polarization curves in 1.0 M KOH under 1600 rpm rotational speed of (b) **C1** and (c) **C2** before and after 5000 cycles stability test (both insets, LSV plots up to current density of 50 mA cm^{-2}); Bar diagram of (d) η_{onset} and (e) $\eta_{10\ mA\ cm^{-2}}$ of before and after 5000 cycle's stability test; (f) OER Tafel plots after 24h stability test.

To confirm the structural stability of **C1** and **C2**, we have run the XPS (Section S2.5; Figures S7 and S8) and elemental analyses (Section S1.2 and

10.1002/anie.202307832

S1.3) which directly prove the presence of the $-Cl^-$ and $-SO_4^{2-}$ ligand in **C1** [Figures S7(a,f)] and **C2** [Figures S8(a,f)], respectively, before and after the catalytic cycle. Additionally, powder-XRD [Section S2.6; Figures S9(a,b)], Raman [Section S2.7; Figures S10(a,b)], cyclic voltammetry (CV) (Section S2.8; Figures S11(a,b)], and SEM analyses [Section S2.9; Figures S12(a,b), S13(a,b)] of **C1** and **C2** are well matched with the initial one (before and after the catalytic cycle) thereby confirming the durability and robustness of the ECs. Furthermore, these result rules out of any chances of oxidation of Cl^- to Cl_2 or oxychloride for **C1** as well as leaching out of SO_4^{2-} in **C2** during OER thereby illustrating the excellent activity of both complexes along with superior durability toward H_2O oxidation. The aforementioned result further confirms the activity as well as the stability trend of our two ECs where **C2** exhibited outstanding activity along with superior durability, illustrating its excellent OER activity among the recently reported top tier OER ECs (Table S3).

In order to investigate the possibility of hydrogen evolution of our Fe-based dinuclear ECs, the electrochemical HER performances of both ECs were evaluated (Section S1.8) and, interestingly, both possess superior HER activities as reflected from Figure 5a. The polarization curve (Figure 5a) of **C2** exhibits a fast raise of cathodic current density with E_{onset} of 39.7 mV which is about 9 mV positive compared to **C1** (Table S4, Figure 5b). Moreover, only 62.0 mV was required for **C2** to attain the current density of 10 mA cm^{-2} which is noticeably lesser than **C1** (74.1 mV), suggesting the higher HER efficiency of **C2**. Additionally, η_{20} for both ECs were also evaluated for the sake of accurate comparison, also showing the similar trend as observed for η_{10} (Table S4). This result demonstrates the admirable HER performance of **C2** compared to **C1** that follows the similar activity trend as OER. Similarly, mass activity of **C2** (Figure 5c) was also observed to be significantly higher where a quite smaller η (110 mV) is needed to obtain a current density of −200 A g^{-1}. Alternatively, **C1** possessed a mass activity of only 112.7 A g^{-1} under the same potential, further illustrating the superior HER activity of **C2** (Figure 5d). Remarkably, Table S5 also reveals **C2** as the best HER electrocatalyst among all recently reported front runners' catalytic systems.

HER activity of **C1** was observed to improve significantly upon replacement of $-Cl^-$ by $-SO_4^{2-}$ indicating the strong substitution effect as well as synergistic effect among the dinuclear Fe and all substituents of the Schiff base ligands. In particular, the enhanced activity of our superior EC, stemming from the synergistic effect, may possibly be ascribed by the following stand points: (i) the enhanced charge transportation as reflected by the EIS (Figure 2b), (ii) abundant active sites as confirmed from large accessible ECSA (Table 1), (iii) ligand conformational effect, and (iv) a strong coupling among dinuclear Fe and Schiff-base ligands. Thus, the developed designed complex EC would create a strong synergistic effect which may decrease the H adsorption energy on EC surface thereby facilitating the HER.

Furthermore, Tafel plots are also used to reveal the inherent reaction pathways as well as to provide insight on the origin of the constantly enhanced activity of **C2**. Figure 5e depicts the comparatively smaller Tafel slope (45.8 mV dec^{-1}) of **C2** than respect to **C1** (Table S4), which reveals the faster HER kinetics on the surface of **C2** with superb e^- transportation. This may due to its large electrocatalytic active sites resulting in superior catalytic performances. Moreover, the Tafel slopes may also suggest hydrogen production *via* the Volmer–Heyrovsky mechanism (Section S1.11, Eq. S8-S9) instead of Tafel pathway (Eq. S10) where electrochemical desorption step is RDS for overall HER (Eq. S11). To further estimate the intrinsic electrocatalytic activity of both ECs, TOF were calculated (Eq. S16) and the superior TOF of **C2** (0.49 s^{-1}) compared to **C1** (0.32 s^{-1}) at constant η of 113 mV further validates the superiority of **C2** toward efficient HER.

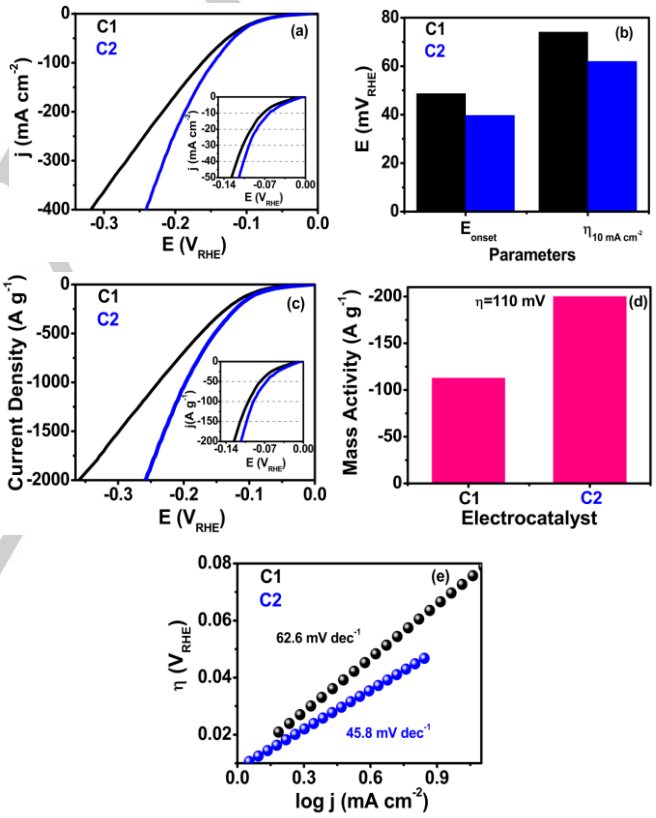

Figure 5. (a) HER polarization curves in 1.0 M KOH under 1600 rpm rotational speed (inset, LSV plot up to current density of -50 mA cm^{-2}), (b) bar diagram representing E_{onset} and $\eta_{10\ mA\ cm^{-2}}$, (c) mass activity plots (inset, plot up to current density of -200 A g^{-1}), (d) bar diagram of mass activity at η=110mV, and (e) the corresponding Tafel plots of both ECs.

The introduction of $-SO_4^{2-}$ ion is highly important for interface engineering to preferentially attract H_2O. Considering the Fe–O (O of SO_4^{2-}) site in **C2**, the −O centre attracts H_2O to the surface through H-bonding which facilitates the H_2O splitting at the Fe site. The moderate electronic configuration of Fe and O sites leads to an easy HO–H bond cleavage with formation of adsorbed H* and Fe-(OH), followed by the removal of –OH to get back its

10.1002/anie.202307832

original structure. Subsequently, another proton from an adjacent H_2O molecule, stabilized by H-bonding, will react with the first H* to generate H_2. Therefore, it is believed that O works in conjunction with the adjacent Fe centre (Fe–OH) to overcome the H_2O dissociation kinetic barrier. Thus, Fe sites and −O groups work co-ordinately to surmount the H_2O dissociation barrier (detailed mechanism in Section S2.11).

From a practical perspective, ECs require an adequate stability to operate at high current density for commercial use. Thus, long–term HER durability was also examined through chronopotentiometric response under constant current of 10 mA cm^{-2}. Figure 6a shows no clear attenuation of η for **C2** during the stability test whereas **C1** experienced a degradation of η after 24 h and this result was further confirmed from the polarization curves after 5000 cycles stability test [Figures 6(b,c)]. As shown in Figure 6e, **C1** possessed ~16.3 mV positive shifted η_{10} while **C2** displays no such change (~0.8 mV) of η_{10} after cycling test (Table S4).

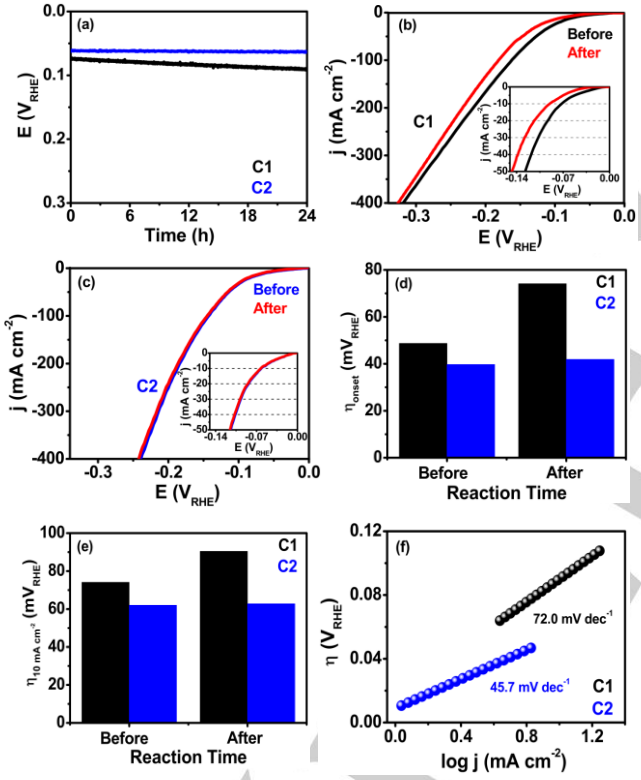

Figure 6. (a) Chronopotentiometric measurements of ECs at 10 mA cm^{-2} for 24 h in 1.0 M KOH under 1600 rpm rotational speed; HER polarization curves in 1.0 M KOH under 1600 rpm rotational speed of (b) **C1** and (c) **C2** before and after 5000 cycles stability test (both insets, LSV plots up to current density of -50 mA cm^{-2}); Bar diagram of (d) η_{onset} and (e) $\eta_{10\ mA\ cm^{-2}}$ of before and after 5000 cycle's stability test; (f) HER Tafel plots after 24h stability test.

The poor durability of **C1** [Figure 6(d,e)] may be attributed to its early degradation, associated to its physical loss or detachment from the electrode's surface during HER. Additionally, the admirable activity and durability of **C2** was also reflected from its almost similar Tafel slope (45.7 mV dec^{-1}) after the stability test whereas **C1** exhibited an increased Tafel slope (Figure 6f). Moreover, the EIS experiment after cycling test further supports their activity trend (Section S2.3, Figures S5). It is worth mentioning from the above results that such admirable HER activity of **C2** with very small η, low Tafel slope and high mass activity made it the best-performing HER electrocatalyst among the current state-of-the-art ECs (Table S5).

Our experimental results demonstrate that the $–Cl^-$ ion in **C1** catalyst is attached to each Fe centre by a single bond while the $–SO_4^{2-}$ ion in **C2** are attached to two Fe centres forming (-O-S-O-) bridge. The larger electronegativity difference between Fe (1.83) and O (3.44) centres compared to Fe and Cl (3.16) as well as the bridging role of the $–SO_4^{2-}$ group synergistically tune the electronic environment of Fe centres which directly facilitates the reactant intermediate adsorption during OER and HER, resulting in an excellent BF H_2O spitting activity. The preference of this chelate linker has demonstrated to promote the intramolecular cooperative effect between the metal centres and forces H_2O molecules to stay as *syn-syn* fashion, thereby promoting O–O bond formation through coupling of neighbouring oxo species and thus reducing the energy barrier for the RDS. Here the oxygen-containing group, $–SO_4^{2-}$ may represents the ligand of choice for surface engineering under the consideration that these groups can form H- bonding with H_2O and attract them to the surface. Moreover, the $–SO_4^{2-}$ ligand electronically activates the Fe centres for –OH adsorption during OER as well as its –O atoms attached to Fe centre attract H_2O molecules closer through H-bonding contributing a reactant friendly interface for facilitation of H_2O splitting in alkaline medium, thus enormously boosting the HER catalytic behaviour of **C2.**

Motivated by the outstanding BF OER and HER performances and admirable durability, a symmetric two electrode alkaline H_2O electrolyzer was assembled using **C2** as both cathodic and anodic material to attain OWS (Section S1.9). Our EC delivered an overall potential of 1.54 V (Figure 7a) to affords a H_2O–splitting current density of 10 mA cm^{-2} which is slightly (20 mV) larger than that of standard Pt/C||RuO_2 [7] but superior than other recently reported ECs (Table S6). Most of the reported molecular OWS catalysts used as nanocatalysts-, are obtained from decomposing molecular metal complexes. Herein, we have directly used the synthesized molecular catalyst for electrocatalytic OWS with excellent bifunctionality thereby reducing the synthetic as well as the operational cost.

As the stability of the molecular ECs is crucial for electrochemical OWS devices, the **C2||C2** electrolyzer was subjected to 24 h of chronopotentiometric stability testing at constant current density of 10 mA cm^{-2} (Figure 7b). The experimental results showed excellent stability with about ~99% potential retention revealing the outstanding robustness of our device. Therefore, the admirable high cathodic current density of 100 mA cm^{-2} at η of just 400 mV as well as the excellent long-term stability make **C2** a as very promising candidate for future energy applications in electrochemical H_2O-splitting devices.

10.1002/anie.202307832

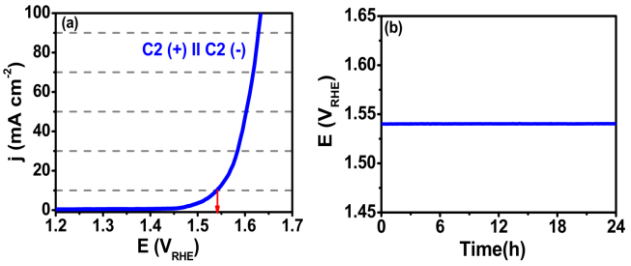

Figure 7. (a) LSV curves of self-assembled alkaline electrolyzers for H_2O electrolysis, and (b) 24 h chronopotentiometric stability test of **C2** based electrolyzer at constant current density of 10 mA cm^{-2}.

The oxygen evolution was further confirmed by controlled-potential electrolysis (CPE) (Figure 8a) at 1.8 V vs NHE (1.6 V vs Ag/AgCl) using a graphite electrode of surface area of 6.4 cm^2 as a working electrode. **C1** and **C2** exhibit constant catalytic current density of 0.011 A cm^{-2} and 0.009 A cm^{-2} (Figure 8a), respectively, throughout the electrolysis. ECs were electrolyzed for 30 minutes at the same potential. For both **C1** and **C2**, the Faraday efficiency for the O_2 evolution is above 90 % (Figure 8b, Table S1). Electrochemical experiments were performed on a CHI-700E electrochemical workstation by a three-electrode system, in which-, a graphite electrode was used as working electrode for controlled potential electrolysis experiments, a platinum wire was the counter electrode, and a Ag/AgCl electrode was the reference electrode. After the electrolysis, the O_2 and H_2 evolved in the head space of the reaction cell were distinguished by GC-TCD chromatography (Section S2.4; Figure S6). Due to their similar thermal conductivities, the sensibility of the GC–TCD for H_2 using helium as a carrier gas is very low.

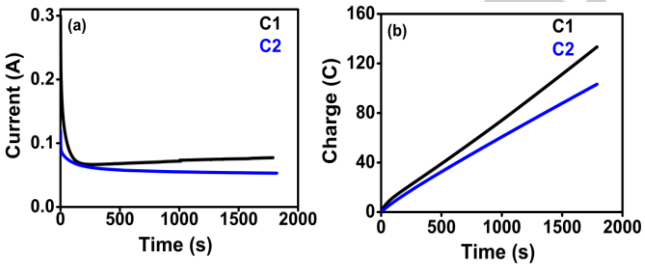

Figure 8. (a) CPE of **C1** and **C2** in 1.0 M KOH (pH ~11.6) solution, and (b) the subsequent O_2 evolution of **C1** and **C2** during the CPE**.**

Thus, the presence of $–SO_4^{2–}$ is considered to play a significant role in regulating the catalytic performance of **C2** through catalytically activating *H and *OH adsorption for H_2O splitting. Herein, **C2** with suitable structural configuration and engineered electronic environment can offer multiple functionalities including abundant active sites and improved conductivity that synergistically contribute to enhanced electrocatalytic BF activity thereby facilitating the H–OH bond cleavage.

Conclusion

In summary, we have designed two efficient and durable heterogeneous BF electrocatalysts using cost-effective Fe salts with a hydrazone-based ligand where the ligand substitution enormously alters the electrocatalytic activity of the molecular catalyst. This strategy may open up a completely new avenue for the design of various new ligand-based H_2O oxidation catalysts that eventually could lead to metal free WSCs. We are confident that the synthetic versatility of molecular transition metal complexes ensured by the large variety of potential ligands that can be used, will lead to rugged and efficient all ligand-based WSCs towards future electrochemical energy conversion.

Acknowledgements

We acknowledge WB-DST for the financial support (Project Memo No 746(Sanc)/ST/P.S&T/15G dt. 22.11.2016.) of this work and the INSPIER fellowship to A.C. (Ref. No. DST/INSPIRE Fellowship/2017/IF170767 dt. 04.07.2018) was funded by DST, New Delhi. SKD also acknowledge the Higher Education Department, Govt. of West Bengal for funding the instrumental facilities to the SKBU including the Raman, XPS, PXRD and SCXRD. We are grateful to the Saha Institute of Nuclear Physics, Kolkata, India for providing the SEM facility and Mr. Debraj De for recording electron images. We sincerely acknowledge Prof. Abhishek Dey of Indian Association for the Cultivation of Science, Kolkata for providing CPE and GC-TCD instrument facilities.

Keywords: Heptacoordinated Fe-complex • Ligand effect • Electrocatalysis • Water splitting • Hydrogen energy

References:

[1] IEA, Paris, "World Energy Outlook 2007", https://www.iea.org/reports/world-energy-outlook-2007, License: CC BY 4.0, **2007**.

[2] G. Zhao, K. Rui, S. X. Dou, W. Sun, *J. Mater. Chem. A* **2020**, *8*, 6393-6405.

[3] Y. Zheng, Y. Jiao, M. Jaroniec, S. Z. Qiao, *Angew. Chem. Int. Ed.* **2015**, *54*, 52-65.

[4] EU Green Deal, Europe, https:// commission.europa.eu/strategy-and-policy/priorities-2019-2024/european-green-deal_en, **2020.**

[5] (a) N. Kuwamura, Y. Kurioka, N. Yoshinari, T. Konno, *Chem. Commun.* **2018**, *54*, 10766-10769; (b) M. Yu, C. Weidenthaler, Y. Wang, E. Budiyanto, E. Onur Sahin, M. Chen, S. DeBeer, O. Rüdiger, H. Tüysüz, *Angew. Chem. Int. Ed.* **2022**, *61*, e202211543.

[6] (a) W. J. Youngblood, S. H. A. Lee, K. Maeda, T. E. Mallouk, *Acc. Chem. Res.* **2009**, *42*, 1966-1973; (b) T. R. Cook, D. K. Dogutan, S.

Y. Reece, Y. Surendranath, T. S. Teets, D. G. Nocera, *Chem. Rev.* **2010**, *110*, 6474-6502; (c) D. Kim, K. K. Sakimoto, D. Hong, P. Yang, *Angew. Chem. Int. Ed.* **2015**, *54*, 3259-3266.

[7] M. Gu, S. C. Wang, C. Chen, D. Xiong, F. Y. Yi, *Inorg. Chem.* **2020**, *59*, 6078-6086.

[8] X. Liang, B. Zheng, L. Chen, J. Zhang, Z. Zhuang, B. Chen, *ACS Appl. Mater. Interfaces* **2017**, *9*, 23222-23229.

[9] Y. Zhao, R. Nakamura, K. Kamiya, S. Nakanishi, K. Hashimoto, *Nat. Commun.* **2013**, *4*, 2390.

[10] (a) X. Wu, F. Li, B. Zhang, L. Sun, *J. Photochem. Photobiol. C: Photochem. Rev.* **2015**, *25*, 71-89; (b) M. D. Kärkäs, B. Åkermark, *Dalton Trans.* **2016**, *45*, 14421-14461.

[11] (a) S. Enthaler, K. Junge, M. Beller, *Angew. Chem. Int. Ed.* **2008**, *47*, 3317-3321; (b) A. Chatterjee, L. K. Thompson, S. K. Dey, *Magnetochemistry*, **2018**, *4*, 53.

[12] P. Garrido-Barros, I. Funes-Ardoiz, S. Drouet, J. Benet-Buchholz, F. Maseras, A. Llobet, *J. Am. Chem. Soc.* **2015**, *137*, 6758-6761.

[13] (a) J. Zhou, W. Xi, J. K. Hurst, *Inorg. Chem.* **1990**, *29*, 160-167; (b) B. Radaram, J. A. Ivie, W. M. Singh, R. M. Grudzien, J. H. Reibenspies, C. E. Webster, X. Zhao, *Inorg. Chem.* **2011**, *50*, 10564-10571; (c) D. Hong, S. Mandal, Y. Yamada, Y. M. Lee, W. Nam, A. Llobet, S. Fukuzumi, *Inorg. Chem.* **2013**, *52*, 9522-9531.

[14] (a) N. D. Schley, J. D. Blakemore, N. K. Subbaiyan, C. D. Incarvito, F. D'Souza, R. H. Crabtree, G. W. Brudvig, *J. Am. Chem. Soc.* **2011**, *133*, 10473-10481; (b) D. W. Shaffer, Y. Xie, J. J. Concepcion, *Chem. Soc. Rev.* **2017**, *46*, 6170-6193; (c) X. J. Su, M. Gao, L. Jiao, R. Z. Liao, P. E. Siegbahn, J. P. Cheng, M. T. Zhang, *Angew. Chem. Int. Ed.* **2015**, *54*, 4909-4914.

[15] (a) S. M. Barnett, K. I. Goldberg, J. M. Mayer, *Nat. Chem.* **2012**, *4*, 498-502; (b) M. T. Zhang, Z. Chen, P. Kang, T. J. Meyer, *J. Am. Chem. Soc.* **2013**, *135*, 2048-2051; (c) Z. Chen, T. J. Meyer, *Angew. Chem. Int. Ed.* **2013**, *52*, 700-703; (d) J. Shen, M. Wang, P. Zhang, J. Jiang, L. Sun, *Chem. Commun.* **2017**, *53*, 4374-4377.

[16] (a) L. A. Stott, K. E. Prosser, E. K. Berdichevsky, C. J. Walsby, J. J. Warren, *Chem. Commun.* **2017**, *53*, 651-654; (b) S. J. Koepke, K. M. Light, P. E. VanNatta, K. M. Wiley, M. T. Kieber-Emmons, *J. Am. Chem. Soc.* **2017**, *139*, 8586-8600; (c) J. Duan, S. Chen, C. Zhao, *Nat. Commun.***2017**, *8*, 15341; (d) L. Sun, M. G. Campbell, M. Dincă, *Angew. Chem. Int. Ed.* **2016**, *55*, 3566-3579.

[17] P. Mondal, J. Satra, D. N. Srivastava, G. R. Bhadu, B. Adhikary, *ACS Catal.* **2021**, *11*, 3687-3703.

[18] C. A. T. J. Li, W. Wan, D. A. Saseendran, Y. Zhao, S. E. Balaghi, S. Heidari, G. R. Patzke, *Chem. Soc. Rev.* **2021**, *50*, 2444-2485.

[19] M. M. Najafpour, A. N. Moghaddam, D. J. Sedigh, M. Hołyńska, *Catal. Sci. Technol.* **2014**, *4*, 30-33.

[20] Y. Liu, R. Xiang, X. Du, Y. Ding, B. Ma, *Chem. Commun.* **2014**, *50*, 12779-12782.

[21] S. Karim, A. Chakraborty, D. Samanta, E. Zangrando, T. Ghosh, D. Das, *Catal. Sci. Technol.* **2020**, *10*, 2830-2837.

[22] D. Wang, L. Que, *Chem. Commun.* **2013**, *49*, 10682-10684.

[23] M. Okamura, M. Kondo, R. Kuga, Y. Kurashige, T. Yanai, S. Hayami, V. K. Praneeth, M. Yoshida, K. Yoneda, S. Kawata, S. Masaoka, *Nature* **2016**, *530*, 465-468.

[24] (a) G. Chen, L. Chen, S. M. Ng, W. L. Man, T. C. Lau, *Angew. Chem. Int. Ed.* **2013**, *52*, 1789-1791; (b) P. Pelosin, M. Gil-Sepulcre, P. Garrido-Barros, D. Moonshiram, J. Benet-Buchholz, C. Gimbert-Suriñach, A. Llobet, *iScience* **2020**, *23*, 101378; (c) J. Serrano-Plana, A. Aguinaco, R. Belda, E. García-España, M. G. Basallote, A. Company, M. Costas, *Angew. Chem. Int. Ed.* **2016**, *55*, 6310-6314; (d) S. Kal, L. Que Jr, *Angew. Chem. Int. Ed.* **2019**, *58*, 8484-8488.

[25] R. H. Holm, P. Kennepohl, E. I. Solomon, *Chem. Rev.* **1996**, *96*, 2239-2314.

[26] C. E. Elwell, N. L. Gagnon, B. D. Neisen, D. Dhar, A. D. Spaeth, G. M. Yee, W. B. Tolman, *Chem.Rev.* **2017**, *117*, 2059-2107.

[27] R. Dhima,C. M. Nagaraja, *Eur. J. Inorg. Chem.* **2018**, *2018*, 2826-2834.

[28] H. M. Lant, T. K. Michaelos, L. S. Sharninghausen, B. Q. Mercado, R. H. Crabtree, G. W. Brudvig, *Eur. J. Inorg. Chem.* **2019**, *2019*, 2115-2123.

[29] Deposition numbers 2238542 (for C1) and 2238543 (for C2) contain the supplementary crystallographic data for this paper. These data are provided free of charge by the joint Cambridge Crystallographic Data Centre and Fachinformationszentrum Karlsruhe Access Structures service, www.ccdc.cam.ac.uk/structures.

[30] A. Bonardi, C. Carini, C. Pelizzi, G. Pelizzi, G. Predieri, P. Tarasconi, M. A. Zoroddu, K. C. Molloy, *J. Organomet. Chem.* **1991**, *401*, 283-294.

[31] I. Vasilevsky, N. Rose, R. Stenkamp, *Acta Cryst. B* **1992**, *48*, 444-449.

[32] C. M. Che, C. W. Chan, S. M. Yang, C. X. Guo, C. Y. Lee, S. M. Peng, J. Chem. Soc., Dalton Trans. **1995**, 2961-2966.

[33] A. Bacchi, I. Ivanovic-Burmazovic, G. Pelizzi, K. Andjelkovic, *Inorg. Chim. Acta* **2001**, *313*, 109-119.

[34] D. M. Doble, A. J. Blake, D. E. Hibbs, M. S. Jackson, W. S. Li, M. Schröder, *Z. anorg. allg. Chem.* **2002**, *628*, 2311-2314.

10.1002/anie.202307832

[35] S. Hannah, V. Lynch, D. M. Guldi, N. Gerasimchuk, C. L. MacDonald, D. Magda, J. L. Sessler, *J. Am. Chem. Soc.* **2002**, *124*, 8416-8427.

[36] S. Sreerama, S. Pal, *Eur. J. Inorg. Chem.* **2004**, *2004*, 4718–4723.

[37] A. Machkour, N. K. Thallaj, L. Benhamou, M. Lachkar, D. Mandon, *Chem. Eur. J.* **2006**, *12*, 6660-6668.

[38] A. Majumder, G. Pilet, M. S. El Fallah, J. Ribas, S. Mitra, *Inorg. Chim. Acta* **2007**, *360*, 2307-2312.

[39] I. V. Korendovych, O. P. Kryatova, W. M. Reiff, E. V. Rybak-Akimova, *Inorg. Chem.* **2007**, *46*, 4197-4211.

[40] G. A. Craig, L. A. Barrios, J. S. Costa, O. Roubeau, E. Ruiz, S. J. Teat, C. C. Wilson, L. Thomas, G. Aromí, *Dalton Trans.* **2010**, *39*, 4874-4881.

[41] M. A. Lemes, A. Pialat, S. N. Steinmann, I. Korobkov, C. Michel, M. Murugesu, *Polyhedron* **2016**, *108*, 163-168.

[42] A. N. Simonson, C. M. Kareis, N. S. Ovanesyan, D. O. Baumann, A. L. Rheingold, A. M. Arif, J. S. Miller, *Polyhedron* **2018**, *139*, 215-221.

[43] T. Shinagawa, A. T. Garcia-Esparza, K. Takanabe, *Sci. Rep.* **2015**, *5*, 13801.

[44] H. T. Zhang, X. J. Su, F. Xie, R. Z. Liao, M. T. Zhang, *Angew. Chem. Int. Ed.* **2021**, *60*, 12467-12474.

10.1002/anie.202307832

Table of Contents

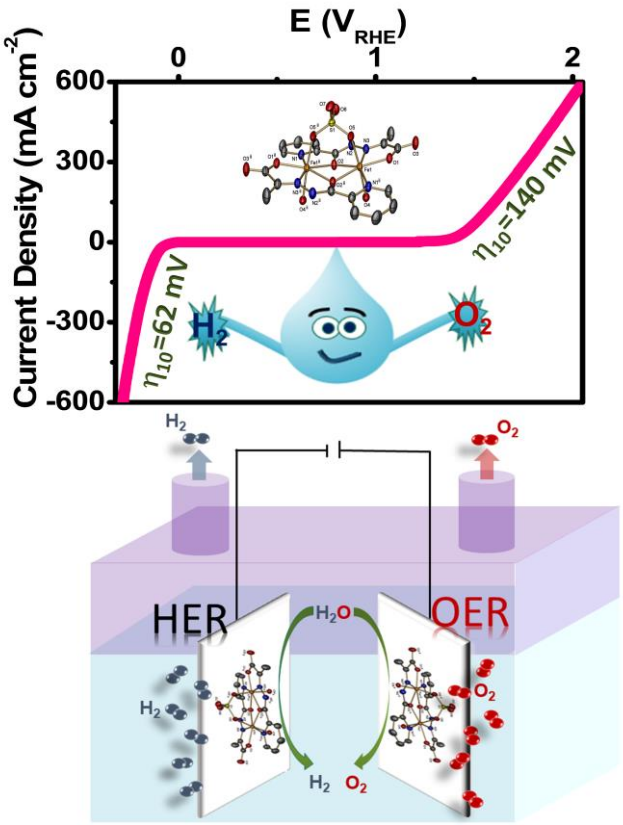

A highly efficient bifunctional electrocatalyst, $[Fe_2L_2(H_2O)_2(SO_4)].2(CH_4O)]$ (**C2**), has been designed to optimize H_2O splitting activity via strategically altering the ligand substitution. The favourable structural conformation with bridging $-SO_4^{2-}$ and engineered electronic environment facilitate the intramolecular oxo–oxo coupling leading to O-O bond formation during electrolysis, effectively enhanced the catalytic functionalities of **C2**.